

High-order \mathcal{C}^1 finite-element interpolating schemes—Part II: Nonlinear semi-Lagrangian shallow-water models

G. Djoumna^{*,†}, D. Y. Le Roux and R. Pierre

Département de Mathématiques et de Statistique, Université Laval, Québec, Canada G1K 7P4

SUMMARY

The finite-element, semi-implicit, and semi-Lagrangian methods are used on unstructured meshes to solve the nonlinear shallow-water system. Several \mathcal{C}^1 approximation schemes are developed for an accurate treatment of the advection terms. The employed finite-element discretization schemes are the $P_1^{\text{NC}}-P_1$ and P_2-P_1 pairs. Triangular finite elements are attractive because of their flexibility for representing irregular boundaries and for local mesh refinement. By tracking the characteristics backward from both the interpolation and quadrature nodes and using \mathcal{C}^1 interpolating schemes, an accurate treatment of the nonlinear terms and, hence, of Rossby waves is obtained. Results of test problems to simulate slowly propagating Rossby modes illustrate the promise of the proposed approach in ocean modelling. Copyright © 2007 John Wiley & Sons, Ltd.

Received 29 June 2007; Revised 12 October 2007; Accepted 14 October 2007

KEY WORDS: characteristic backward tracking; shallow-water equations; finite elements; semi-Lagrangian methods

1. INTRODUCTION

Free surface flows are encountered in a wide variety of natural phenomena, such as the description of hydrodynamic currents, the transport of pollutant, and the evolution of oceanic and atmospheric flows. The first numerical ocean models [1, 2] employed finite difference techniques and a leapfrog scheme for time integration. The use of Galerkin-type methods in ocean modelling has been an active area of research for the last three decades. The main advantages of these methods are a natural treatment of boundary conditions and the flexibility of triangulation for representing the boundaries

*Correspondence to: Georges Djoumna, Département de Mathématiques et de Statistique, Université Laval, Québec, Canada G1K 7P4.

†E-mail: gdjoumna@giref.ulaval.ca, gdjoumna@mat.ulaval.ca

Contract/grant sponsor: Natural Sciences and Engineering Research Council (NSERC)

Contract/grant sponsor: Fonds québécois de la recherche sur la nature et les technologies (FQRNT)

of complex domains and local mesh refinement. Their inherent grid flexibility in representing steep gradients in currents and bathymetry offers a significant advantage to simulate nearshore and coastal processes. Shallow-water equations have been first solved for coastal dynamics and global ocean tide modelling [3–5]. Three-dimensional hydrostatic models have then been developed for large-scale circulation using spectral elements [6], finite volumes [7, 8], and finite elements (FE) [9–11]. A three-dimensional nonhydrostatic ocean model designed for both large- and small-scale applications has also been developed [12]. The discontinuous Galerkin (DG) method [13, 14] has been recently employed to discretize the shallow-water system [15–17]. Advantages of the DG method include the local mass conservation and the possibility of employing high-order and discontinuous basis functions.

Eulerian advection schemes are widely used for large-scale ocean models. For such schemes, the accuracy of the nonlinear advection terms, and thus of the slow planetary or Rossby modes, is determined by the order of spatial approximation. For advection-dominated problems, a high-order spatial accuracy is desirable for the treatment of the Rossby modes. Indeed, Rossby waves play an important role in the adjustment of oceanic and atmospheric flows. They propagate energy westward and are responsible for the westward intensification associated with western boundary currents in the large-scale oceanic circulation [18]. When continuous FE are employed, Eulerian advection schemes usually suffer from significant numerical dispersion. This results in the use of unphysical diffusion to keep the solution coherent and can adversely affect the accuracy of the Rossby modes for long-term integrations. When DG formulations are used, the dispersion effects are attenuated due to the higher flexibility of these methods that makes them better suited to represent highly sheared flows [19].

In an FE context, both the accuracy and dispersion difficulties encountered with an Eulerian scheme should, in principle, be circumvented by combining the FE scheme with a semi-Lagrangian treatment of advection. Such a combination should benefit from the flexibility of FE meshes, the small numerical dispersion of a semi-Lagrangian scheme, and the possibility of a high-order treatment of the advection terms. Furthermore, the semi-Lagrangian scheme offers the possibility of using time steps that exceed those permitted by the Courant–Friedrichs–Lewy (CFL) stability criterion for Eulerian discretizations of advection-dominated flows. Note that in [20] the continuity equation is discretized in an Eulerian manner to conserve mass while the momentum equations are solved using semi-Lagrangian advection.

In the present study, a semi-Lagrangian method using high-order \mathcal{C}^1 interpolating schemes based on the Hsieh–Clough–Tocher and Bell elements and the FE method employing the P_2 – P_1 and P_1^{NC} – P_1 pairs are combined to solve the shallow-water equations on unstructured meshes. Two semi-Lagrangian methods are considered by tracking the feet of the characteristic lines either from the interpolation or from the integration nodes. In [21–24], the P_1^{NC} – P_1 pair has been found a good candidate to discretize both inertia-gravity and Rossby waves. High-order \mathcal{C}^1 schemes are employed in [25] in the case of the two-dimensional linear advection equation, and the dual kriging method has been used in [21, 26] for the semi-Lagrangian advection.

The aim of this paper is to develop an accurate semi-Lagrangian method for ocean modelling. This paper is organized as follows. In Section 2, the model equations are presented, and in Sections 3 and 4, the time and space discretizations are, respectively, described. Results of test experiments to simulate slowly propagating Rossby modes and aiming to outline the accuracy of the proposed methods are presented in Section 5. Some concluding remarks complete the study.

2. THE NONLINEAR SHALLOW-WATER EQUATION MODEL

Let Ω be a bounded domain in the two-dimensional space \mathbb{R}^2 with Lipschitz boundary Γ , g the gravitational acceleration, \mathbf{k} the unit vector in the vertical, and f the Coriolis parameter. Consider an inviscid layer of constant and uniform density. The nonlinear inviscid shallow-water equations in Cartesian coordinates [27] are expressed in logarithmic form as

$$\frac{D\mathbf{u}}{Dt} + g\nabla\eta + f\mathbf{k} \wedge \mathbf{u} = 0 \tag{1}$$

$$\frac{D \ln(H + \eta)}{Dt} + \nabla \cdot \mathbf{u} = 0 \tag{2}$$

where D/Dt is the total or Lagrangian derivative

$$\frac{D}{Dt} = \frac{\partial}{\partial t} + \mathbf{u} \cdot \nabla \tag{3}$$

$\mathbf{u} = (u, v)$ is the horizontal mean velocity field, \wedge is the usual vector product, $\eta(\mathbf{x}, t)$ represents the surface elevation above the reference level $z=0$, and $\mathbf{x} = (x, y)$ is the position vector. The equilibrium depth is denoted by $H(\mathbf{x})$ and the rigid bottom is defined by $z = -H(\mathbf{x})$. Further, the total depth $\eta + H$ is supposed to be positive. System (1) is solved under the no-normal-flow boundary condition:

$$\mathbf{u} \cdot \mathbf{n} = 0 \quad \text{on } \Gamma \tag{4}$$

where \mathbf{n} is the unit outward-pointing normal at the boundary Γ .

3. TEMPORAL SEMI-DISCRETIZATION

A linear analysis of (1)–(2) reveals three solution frequencies per wave number. The first two are fast inertia-gravitational modes, while the third is the Rossby mode, the mode of principal interest here. For many geophysical flows, gravity modes usually carry relatively little energy compared with the Rossby modes of the large-scale dynamics. However, when an explicit time discretization scheme is used, e.g. the leapfrog scheme, the time step is limited by the propagation speed of gravitational oscillations. In an atmospheric context [28, 29], a semi-implicit treatment of the linear terms responsible for the rapidly propagating gravitational oscillations allows much larger time steps. The semi-implicit scheme reduces the phase speed of these fast disturbances without modifying their amplitude. Unless an accurate representation of the fast modes is important, gravity waves may be considered as small-amplitude noise superimposed on the slow Rossby mode, and they can justifiably be retarded by a semi-implicit scheme.

The maximum allowable time step, when using a semi-implicit scheme, still remains much smaller than that based on accuracy consideration alone and is constrained by the CFL bound associated with Eulerian advection. For advection-dominated flows, a semi-Lagrangian treatment of advection combined with a semi-implicit scheme permits stable solutions with large time steps. The possibility of stable integration with CFL greater than unity is not the only advantage of a semi-Lagrangian advection scheme. It also gives good phase speeds with little numerical dispersion compared with Eulerian schemes. However, due to the compulsory spatial reinterpolation

of the semi-Lagrangian method, some damping does occur, affecting primarily the smallest scales, provided sufficiently high-order interpolators are used [26, 30].

Let T be a positive real number and consider a partition of the time interval $[0, T]$ into N subintervals $[t_n, t_{n+1}]$, with $\Delta t = t_{n+1} - t_n$ for $n = 0, 1, \dots, N - 1$. Let m, n be two positive integers and define

$$\mathbf{u}_m^{n+1} \equiv \mathbf{u}(\mathbf{x}_m, t_n + \Delta t), \quad \mathbf{u}_{\alpha_m}^n \equiv \mathbf{u}(\mathbf{x}_m - \alpha_m, t_n) \tag{5}$$

A schematic of the one-dimensional two-time-level semi-Lagrangian scheme [31, 32] is described in Figure 1. A different set of particles is selected at each time step, and the particles are required to arrive at mesh nodes at the end of the time step. The straight line ($A'C$) approximates the exact trajectory (AC), both of which arrive at mesh point x_m at time $t_n + \Delta t$. The particle is displaced by the distance α_m during the time Δt . The total time derivative at mesh nodes is the rate of change along flow characteristics, and the semi-Lagrangian advection thus uses time differences along particle trajectories. The other terms in (1)–(2) are treated in a semi-implicit manner as time averages along these trajectories, and we obtain

$$\frac{\mathbf{u}_m^{n+1} - \mathbf{u}_{\alpha_m}^n}{\Delta t} + \frac{g}{2}(\nabla \eta_m^{n+1} + \nabla \eta_{\alpha_m}^n) + \frac{1}{2}f(\mathbf{k} \wedge \mathbf{u}_m^{n+1} + f\mathbf{k} \wedge \mathbf{u}_{\alpha_m}^n) = 0 \tag{6}$$

$$\frac{[\ln(H + \eta)]_m^{n+1} - [\ln(H + \eta)]_{\alpha_m}^n}{\Delta t} + \frac{1}{2}(\nabla \cdot \mathbf{u}_m^{n+1} + \nabla \cdot \mathbf{u}_{\alpha_m}^n) = 0 \tag{7}$$

For the sake of simplicity, we let

$$[\mathbf{R}^u]_{\alpha_m}^n = \mathbf{u}_{\alpha_m}^n - g \frac{\Delta t}{2} \nabla \eta_{\alpha_m}^n - \frac{\Delta t}{2} \mathbf{k} \wedge f \mathbf{u}_{\alpha_m}^n \tag{8}$$

$$[R^\eta]_{\alpha_m}^n = [\ln(H + \eta)]_{\alpha_m}^n - \frac{\Delta t}{2} \nabla \cdot \mathbf{u}_{\alpha_m}^n \tag{9}$$

and (6)–(7) are rewritten as

$$\mathbf{u}_m^{n+1} + g \frac{\Delta t}{2} \nabla \eta_m^{n+1} + \frac{\Delta t}{2} \mathbf{k} \wedge f \mathbf{u}_m^{n+1} = [\mathbf{R}^u]_{\alpha_m}^n \tag{10}$$

$$[\ln(H + \eta)]_m^{n+1} + \frac{\Delta t}{2} \nabla \cdot \mathbf{u}_m^{n+1} = [R^\eta]_{\alpha_m}^n \tag{11}$$

To compute the right-hand sides (RHS) of (10) and (11), we need to evaluate $[\mathbf{R}^u]_{\alpha_m}^n$ and $[R^\eta]_{\alpha_m}^n$. We first determine α_m by approximate integration of the displacement equation $D\mathbf{x}/Dt = \mathbf{u}(\mathbf{x}, t)$ that defines the trajectories. A first-order estimate $\alpha_m^0 = \Delta t \mathbf{u}(\mathbf{x}_m, t_n)$ is combined with several iterations of a second-order Runge–Kutta corrector:

$$\alpha_m^{k+1} = \Delta t \mathbf{u}^* \left(\mathbf{x}_m - \frac{\alpha_m^k}{2}, t_n + \frac{\Delta t}{2} \right), \quad k = 1, 2, 3, \dots \tag{12}$$

using interpolation when evaluating the RHS. In order to have sufficiently accurate $O(\Delta t^2)$ estimates of the trajectory, a two-time-level scheme [31, 32] (see Figure 1) extrapolates the velocity

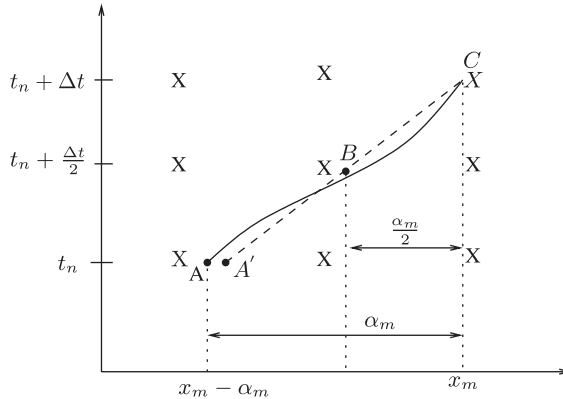


Figure 1. A two-level semi-Lagrangian advection scheme. Approximated ($A'C$) and exact (AC) trajectories arrive at node x_m at time $t_n + \Delta t$. The particle is displaced by the distance α_m during the time Δt .

field at all nodes at time $(t_n + \Delta t/2)$:

$$\mathbf{u}^* \left(\mathbf{x}, t_n + \frac{\Delta t}{2} \right) = \frac{3}{2} \mathbf{u}(\mathbf{x}, t_n) - \frac{1}{2} \mathbf{u}(\mathbf{x}, t_n - \Delta t) + O(\Delta t^2) \tag{13}$$

Finally, $[\mathbf{R}^u]_{\alpha_m}^n$ and $[R^\eta]_{\alpha_m}^n$ are computed by using an interpolator. The choice of an interpolating scheme has a crucial impact on the accuracy of the method, and this question is addressed in the following section.

4. FE DISCRETIZATION

4.1. The weak formulation

We assume that \mathbf{u}_m and η_m belong to the spaces \mathcal{V} and \mathcal{Q} , respectively, with \mathcal{Q} and \mathcal{V} being either the square-integrable space $L^2(\Omega)$ or the Sobolev space $H^1(\Omega)$, i.e. the space of functions in $L^2(\Omega)$ whose first derivatives belong to $L^2(\Omega)$. The weak formulation of (10) and (11) requires the test functions Φ and Ψ to be sufficiently regular and to, respectively, belong to the same function space as \mathbf{u}_m and η_m , such that

$$\int_{\Omega} \mathbf{u}_m^{n+1} \cdot \Phi \, d\Omega + g \frac{\Delta t}{2} \int_{\Omega} \nabla \eta_m^{n+1} \cdot \Phi \, d\Omega + \frac{\Delta t}{2} \int_{\Omega} f \mathbf{k} \wedge \mathbf{u}_m^{n+1} \cdot \Phi \, d\Omega = \int_{\Omega} [\mathbf{R}^u]_{\alpha_m}^n \cdot \Phi \, d\Omega \tag{14}$$

$$\int_{\Omega} [\ln(H + \eta)]_m^{n+1} \Psi \, d\Omega + \frac{\Delta t}{2} \int_{\Omega} \nabla \cdot \mathbf{u}_m^{n+1} \Psi \, d\Omega = \int_{\Omega} [R^\eta]_{\alpha_m}^n \Psi \, d\Omega \tag{15}$$

where the area element is $d\Omega = dx \, dy$.

Depending on the regularity of functions \mathbf{u}_m and η_m , the terms containing derivatives in (14) and (15) may be integrated by parts using Green's theorem, by letting $\mathbf{u}_m \cdot \mathbf{n} = 0$ on Γ for all \mathbf{u}_m belonging to \mathcal{V} .

4.2. Galerkin FE discretization

The Galerkin method approximates the solution of (14) and (15) in finite-dimensional subspaces. Consider an FE triangulation \mathcal{L}_h of the polygonal domain Ω , where h is a representative meshlength parameter that measures resolution. For triangle $K \in \mathcal{L}_h$, let $P_n(K)$ denote the space of polynomials of degree n on K .

The discrete solutions \mathbf{u}_h and η_h sought belong to finite-dimensional spaces \mathcal{V}_h and \mathcal{Q}_h , respectively, whose restrictions on K belong to $P_k(K) \times P_k(K)$ for \mathbf{u}_h and to $P_l(K)$ for η_h . The quantities \mathbf{u}_h and η_h are represented over a triangle K by interpolating functions Φ_k of degree k and Ψ_l of degree l , respectively, with Φ_k belonging to \mathcal{V}_h and Ψ_l belonging to \mathcal{Q}_h . Introducing the FE basis leads to an FE statement as in (14) and (15) but with \mathbf{u}_m, η_m replaced by the FE trial functions \mathbf{u}_h, η_h and Φ_k and Ψ_l replaced by the corresponding FE test functions. The resulting system is nonlinear due to the presence of the logarithmic term in the left-hand side (LHS) of the continuity equation and it is solved by applying Newton’s method. To do so, the Gâteaux derivative of the logarithmic term on the LHS of (15) is formally computed.

4.3. Newton–Raphson procedure

Let p and p_{\max} be two integers. For $p=0, \dots, p_{\max}$, we set $\mathbf{u}_h^{n+1,p+1} = \mathbf{u}_h^{n+1,p} + \delta \mathbf{u}_h^p$ and $\eta_h^{n+1,p+1} = \eta_h^{n+1,p} + \delta \eta_h^p$. For a given initial guess $(\mathbf{u}_h^{n+1,0}, \eta_h^{n+1,0})$ and $p=0, \dots, p_{\max}$, Newton–Raphson’s procedure aims at the determination of $(\delta \mathbf{u}_h^p, \delta \eta_h^p)$ such that

$$\int_{\Omega} \delta \mathbf{u}_h^p \cdot \Phi_k \, d\Omega + g \frac{\Delta t}{2} \int_{\Omega} \nabla \delta \eta_h^p \cdot \Phi_k \, d\Omega + \frac{\Delta t}{2} \int_{\Omega} f \mathbf{k} \wedge \delta \mathbf{u}_h^p \cdot \Phi_k \, d\Omega = F_{\mathbf{u}}(\mathbf{u}_h^{n+1,p}, \eta_h^{n+1,p}, [\mathbf{R}^{\mathbf{u}}]_{\alpha_m}^n) \tag{16}$$

$$\int_{\Omega} \frac{\delta \eta_h^p}{H + \eta_h^{n+1}} \Psi_l \, d\Omega + \frac{\Delta t}{2} \int_{\Omega} \nabla \cdot \delta \mathbf{u}_h^p \Psi_l \, d\Omega = F_{\eta}(\mathbf{u}_h^{n+1,p}, \eta_h^{n+1,p}, [R^{\eta}]_{\alpha_m}^n) \tag{17}$$

where

$$F_{\mathbf{u}}(\mathbf{u}_h^{n+1,p}, \eta_h^{n+1,p}, [\mathbf{R}^{\mathbf{u}}]_{\alpha_m}^n) \equiv \int_{\Omega} \mathbf{u}_h^{n+1,p} \cdot \Phi_k \, d\Omega + g \frac{\Delta t}{2} \int_{\Omega} \nabla \eta_h^{n+1,p} \cdot \Phi_k \, d\Omega + \frac{\Delta t}{2} \int_{\Omega} f \mathbf{k} \wedge \mathbf{u}_h^{n+1,p} \cdot \Phi_k \, d\Omega - \int_{\Omega} [\mathbf{R}^{\mathbf{u}}]_{\alpha_m}^n \cdot \Phi_k \, d\Omega \tag{18}$$

and

$$F_{\eta}(\mathbf{u}_h^{n+1,p}, \eta_h^{n+1,p}, [R^{\eta}]_{\alpha_m}^n) \equiv \int_{\Omega} [\ln(H + \eta)]_h^{n+1,p} \Psi_l \, d\Omega + \frac{\Delta t}{2} \int_{\Omega} \nabla \cdot \mathbf{u}_h^{n+1,p} \Psi_l \, d\Omega - \int_{\Omega} [R^{\eta}]_{\alpha_m}^n \Psi_l \, d\Omega \tag{19}$$

4.4. P_2 - P_1 and P_1^{NC} - P_1 FE formulations

We now introduce the FE schemes that are used for the spatial discretization. Two candidates of FE pair for representing velocity and surface elevation are described and evaluated in the remainder of this paper. Common to the two pairs is piecewise-linear continuous representation of surface elevation, and they differ from one another in their representation of velocity. The P_2 - P_1 pair [33], also known in the literature as the Taylor–Hood element, has quadratic velocity basis functions. The P_1^{NC} - P_1 pair [22–24, 34] has velocity nodes at triangle edge midpoints, and linear basis functions are used to approximate the two velocity components on the element’s two-triangle support. Since this particular representation of velocity is continuous only across triangle boundaries at midpoint nodes and discontinuous everywhere else around a triangle boundary, this element is termed nonconforming (NC) in the FE literature. The orthogonality property of the NC velocity basis functions leads to diagonal mass matrices and thus greatly enhances computational efficiency.

The space \mathcal{V}_h is the set of functions \mathbf{u}_h whose restriction on K belongs to $P_2(K) \times P_2(K)$ for the P_2 - P_1 pair and to $P_1(K) \times P_1(K)$ for the P_1^{NC} - P_1 one, with \mathbf{u}_h being continuous only at the midpoints of each face of \mathcal{L}_h for the latter pair. For both pairs we have $\mathbf{u}_h \cdot \mathbf{n} = 0$ on Γ . To avoid computing velocity derivatives for the P_1^{NC} - P_1 approximation, the divergence terms appearing in (15) and hence (17) are integrated by parts using Green’s theorem. In this way, only Ψ derivatives are required and not Φ derivatives.

To calculate $[\mathbf{R}^u]_{\alpha_m}^n$ and $[R^\eta]_{\alpha_m}^n$ in (16) and (17), two semi-Lagrangian methods are considered. In the first case, one uses the characteristic stemming backward from the interpolation nodes, named here as *interpolation semi-Lagrangian FE method* (ISLFEM), while in the second case one uses those stemming from the quadrature nodes, named here as *quadrature semi-Lagrangian FE method* (QSLFEM). These methods are described in [25] in the case of the two-dimensional linear advection equation, and they are now briefly reviewed in the present context.

4.5. Interpolation and quadrature semi-Lagrangian FE methods

The ISLFEM procedure evaluates the integrals in the RHS of (16) and (17) following the five-step process:

- (i) Obtain $[\mathbf{R}^u]^n$ and $[R^\eta]^n$ at each node at time t_n .
- (ii) Evaluate the displacement α_m at each *interpolation* node at time t_n using (12).
- (iii) Compute $[\mathbf{R}^u]^n$ and $[R^\eta]^n$ at the upstream positions $\mathbf{x}_m - \alpha_m$ by using an interpolation scheme to obtain $[\widehat{\mathbf{R}}^u]^n$ and $[\widehat{R}^\eta]^n$.
- (iv) Expand $[\widehat{\mathbf{R}}^u]^n$ and $[\widehat{R}^\eta]^n$ in terms of the basis functions as $[\widehat{\mathbf{R}}^u]^n = \sum_i [\widehat{\mathbf{R}}^u]_i^n \cdot \Phi_i$ and $[\widehat{R}^\eta]^n = \sum_j [\widehat{R}^\eta]_j^n \Psi_j$ on each triangle K of \mathcal{L}_h .
- (v) Compute the integral in the RHS of (16) and (17) by employing a numerical quadrature:

$$\int_K [\mathbf{R}^u]_{\alpha_m}^n \cdot \Phi_k \, d\Omega = \sum_i \sum_q \omega_q [\widehat{\mathbf{R}}^u]_i^n \Phi_i(\xi_q) \cdot \Phi_k(\xi_q) \tag{20}$$

$$\int_\Omega [R^\eta]_{\alpha_m}^n \Psi_l \, d\Omega = \sum_j \sum_q \omega_q [\widehat{R}^\eta]_j^n \Psi_j(\xi_q) \Psi_l(\xi_q) \tag{21}$$

where ω_q and ξ_q are the weights and points of the used quadrature formula, respectively.

For the QSLFEM, the algorithm is completed following the four-step process:

- (i) Obtain $[\mathbf{R}^u]^n$ and $[R^\eta]^n$ at each node at time t_n as for the ISLFEM.
- (ii) Evaluate the displacement α_m at each *integration* node at time t_n using (12).
- (iii) Compute $[\mathbf{R}^u]_{\alpha_m}^n$ and $[R^\eta]_{\alpha_m}^n$ at the upstream points $\xi_q - \alpha_m(\xi_q)$ by using an interpolation scheme.
- (iv) Compute the integral in the RHS of (16) and (17) by employing a numerical quadrature

$$\int_K [\mathbf{R}^u]_{\alpha_m}^n \cdot \Phi_k \, d\Omega = \sum_q \omega_q [\mathbf{R}^u]^n(\xi_q - \alpha_m(\xi_q)) \Phi(\xi_q) \cdot \Phi_k(\xi_q) \quad (22)$$

$$\int_\Omega [R^\eta]_{\alpha_m}^n \Psi_l \, d\Omega = \sum_q \omega_q [R^\eta]^n(\xi_q - \alpha_m(\xi_q)) \Psi(\xi_q) \Psi_l(\xi_q) \quad (23)$$

The accuracy of the nonlinear terms mainly derives from the semi-Lagrangian treatment of advection in the present formulation and not from the accuracy of the FE scheme. Furthermore, a semi-implicit scheme is used to discretize the terms responsible for the rapidly propagating gravitational oscillations and also for the Coriolis terms. The calculation of $[\mathbf{R}^u]_{\alpha_m}^n$ and $[R^\eta]_{\alpha_m}^n$ in (16) and (17), and hence the accuracy of the method, strongly depends on the choice of the interpolation procedure at step (iii) for the ISLFEM and the QSLFEM, respectively. The bicubic spline interpolation has been found to be a good compromise between accuracy and computational cost for short-term simulations in the context of atmospheric models [31, 35, 36]. For oceanic models, where long-term simulations are of primary importance, bicubic spline interpolation could introduce undesirable dissipation. In [26, 37] the kriging method has been used as a proof-of-concept test and was found to yield equally high-order accuracy results on regular grids and unstructured meshes. Here, we employed a class of \mathcal{C}^1 FE interpolating schemes based on the Hsieh–Clough–Tocher FE reduced and complete, named here as HCT-C and HCT-R, respectively, and the Bell family. These schemes are detailed in [25] in the case of the two-dimensional linear advection equation, and they give comparable numerical results as the kriging scheme on structured meshes. In the sequel, the use of \mathcal{C}^1 -interpolating schemes on unstructured meshes is investigated.

4.6. The boundary condition

At a boundary node, the no-normal-flow condition (4) needs to be applied across element boundary, which is not necessarily parallel to the Cartesian coordinate axes. For the $P_1^{\text{NC}}-P_1$ pair, velocity nodes are located at triangle midedge points, and hence the local normal vector is uniquely defined along the boundary. However, this is not the case for the conforming P_2-P_1 pair since velocity nodes are in part located at the vertices.

This problem has been addressed by Gray [38] for the case of the shallow-water equations. In the present work, we employ the normal to the boundary defined as follows: given a boundary node, a regular surface is constructed using all the elements that share the given node, and we consider the normal to that surface. The momentum equations corresponding to a boundary node in (16) are then transformed into tangential and normal equations. The local x - y coordinate system at this node is rotated to coincide with the tangential and normal directions, and the no-normal-flow boundary condition is applied [39].

5. NUMERICAL EXPERIMENTS

The results of two tests using the combination of the FE, semi-implicit, and semi-Lagrangian methods are now presented. The P_2-P_1 and $P_1^{NC}-P_1$ pairs are used for the FE method, and the semi-Lagrangian advection employed the ISLFEM and the QSLFEM with \mathcal{C}^1 -interpolating schemes. In both tests, the slowly propagating Rossby modes are simulated and the model is run as a reduced-gravity model with parameters set to correspond to the first internal vertical mode of a baroclinic model. This formulation precludes any influence of the bathymetry, and the mean depth H is therefore set constant in the simulations.

5.1. Equatorial Rossby soliton

In the first experiment the propagation of an equatorial solitary Rossby wave is examined. Equatorial solitons are confined to a narrow band about the equator by Coriolis forces, and they should preserve their shape while travelling westward at a constant phase speed in the absence of dissipation. The goal of this experiment is to reproduce numerically the main characteristics of such a propagation. The β -plane approximation, $f = f_0 + \beta y$, is used, where $f_0 = 2\Omega \sin \varphi_0$ is the reference Coriolis parameter, $\beta = 2(\Omega/R) \cos \varphi_0$ is the β -parameter, and R and Ω are the Earth's radius and the angular frequency of the Earth's rotation, respectively. We introduce the adimensional variables:

$$\mathbf{x} = L\mathbf{x}', \quad t = Tt', \quad \mathbf{u} = U\mathbf{u}', \quad \eta = H\eta' \tag{24}$$

where $L = RE^{-1/4}$, $T = E^{1/4}(2\Omega)^{-1}$, $U = \sqrt{g'H}$, and $E = (2\Omega)^2/(g'H)$ is the Lamb number. By taking $g' = 4 \times 10^{-2} \text{ m s}^{-2}$ and $H = 100 \text{ m}$, the gravity wave speed is $U = 2 \text{ m s}^{-1}$, and it corresponds to the wave speed of the first baroclinic mode. Those values yield a length scale of 296 km and a time scale of 41 h. By substituting the adimensional variables from (24) into (1) and (2) and omitting the primes, the shallow-water system is obtained on an equatorial β -plane (i.e. for $\varphi_0 = 0$) in a reduced gravity form:

$$\frac{D\mathbf{u}}{Dt} + \nabla\eta + y\mathbf{k} \wedge \mathbf{u} = 0 \tag{25}$$

$$\frac{D \ln(1+\eta)}{Dt} + \nabla \cdot \mathbf{u} = 0 \tag{26}$$

which is solved subject to the no-normal boundary condition (4). The rectangular domain extent is 32×8 adimensional units. The mesh resolution is $h' = 0.5$ in the refined region and $h' = 1$ elsewhere in adimensional unit with $h' = h/L$. To balance the temporal and spatial truncation errors, we choose $\Delta t' = 0.25$ adimensional time unit, and the gravitational Courant number is thus $c \equiv UT\Delta t'/(h'L) \approx 1$, where h' is defined to be the distance between a midside node and an adjacent vertex node. The mesh used for the experiment is shown in Figure 2.

The velocity field and the surface elevation at the initial time are

$$u(x, y, t = 0) = AB^2 \frac{(6y^2 - 9)}{4} \text{sech}^2(Bx) \exp\left(\frac{-y^2}{2}\right) \tag{27}$$

$$v(x, y, t = 0) = -4AB^3 y \tanh(Bx) \text{sech}^2(Bx) \exp\left(\frac{-y^2}{2}\right) \tag{28}$$

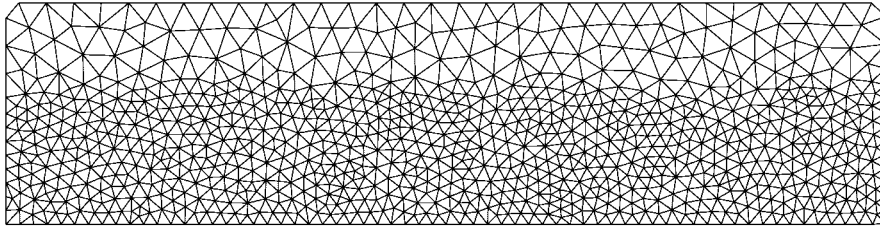


Figure 2. The mesh used in the equatorial Rossby soliton experiment.

$$\eta(x, y, t=0) = AB^2 \frac{(6y^2+3)}{4} \operatorname{sech}^2(Bx) \exp\left(\frac{-y^2}{2}\right) \quad (29)$$

For this experiment the P_2 - P_1 and P_1^{NC} - P_1 pairs lead to very close solutions and only the results for the P_2 - P_1 pair are presented. At the beginning of the simulation, the surface elevation loses approximately 5% of its initial amplitude, which propagates eastward as equatorial Kelvin waves. This is because the initial condition is not an exact solitary solution. Meanwhile the equatorial solitary Rossby wave propagates westward. The ISLFEM and the QSLFEM are used for three classes of \mathcal{C}^1 interpolators: the HCT-R, HCT-C, and Bell approximation schemes. The isolines of the surface elevation are shown in Figures 3 and 4 after 55 days of integration (32 adimensional time units) for these methods.

For the ISLFEM, the soliton exhibits small-amplitude noise for the HCT-R and HCT-C schemes, as shown in Figure 3. For the Bell approximation, the solution is much more noisy and the soliton has almost lost its initial shape. Much better results are obtained in Figure 4 for the QSLFEM since the equatorial soliton propagates westward with little change in shape. Note that a severe damping of the solution occurs for the ISLFEM with the HCT-R and HCT-C schemes. The phase velocity is shown in Table I and could be compared with the asymptotic solution of Boyd [40] which predicts a value of 0.78 ms^{-1} . The QSLFEM results are very satisfactory and they compare well with those obtained in [21] using the P_1^{NC} - P_1 pair and the kriging scheme for the ISLFEM.

An important issue in the discretization of the shallow-water system is mass conservation. The mass variation (MV), defined as $MV \equiv \int_{\Omega} \eta(\mathbf{x}, t) d\Omega / \int_{\Omega} \eta(\mathbf{x}, t=0) d\Omega$, is shown in Figures 5 and 6 for the ISLFEM and the QSLFEM after 55 days of simulation. For the ISLFEM, we obtain $MV = 0.81$ and 0.75 for the HCT (HCT-R and HCT-C) and Bell approximations, respectively. The loss of mass is thus significant (19 and 25% for the HCT and Bell schemes, respectively). For the QSLFEM, $MV = 0.993$, 0.9955 , and 0.9963 for the HCT-R, HCT-C, and Bell approximations, respectively, and the loss of mass is thus less than 1%. These results clearly show that the QSLFEM better conserves mass than the ISLFEM in the present context.

5.2. Anticyclonic eddy propagation

For the second test problem, the slowly propagating Rossby modes are simulated in the case of the evolution of an anticyclonic eddy at midlatitudes. The computational domain is a realistic geometry of the Gulf of Mexico and it is approximately $1800 \text{ km} \times 1350 \text{ km}$. The mesh is shown in Figure 7 with a resolution of 20 km in the western part of the Gulf and 60 km in the eastern part. The basin is assumed to be closed. Although this experiment is highly idealized, it is expected

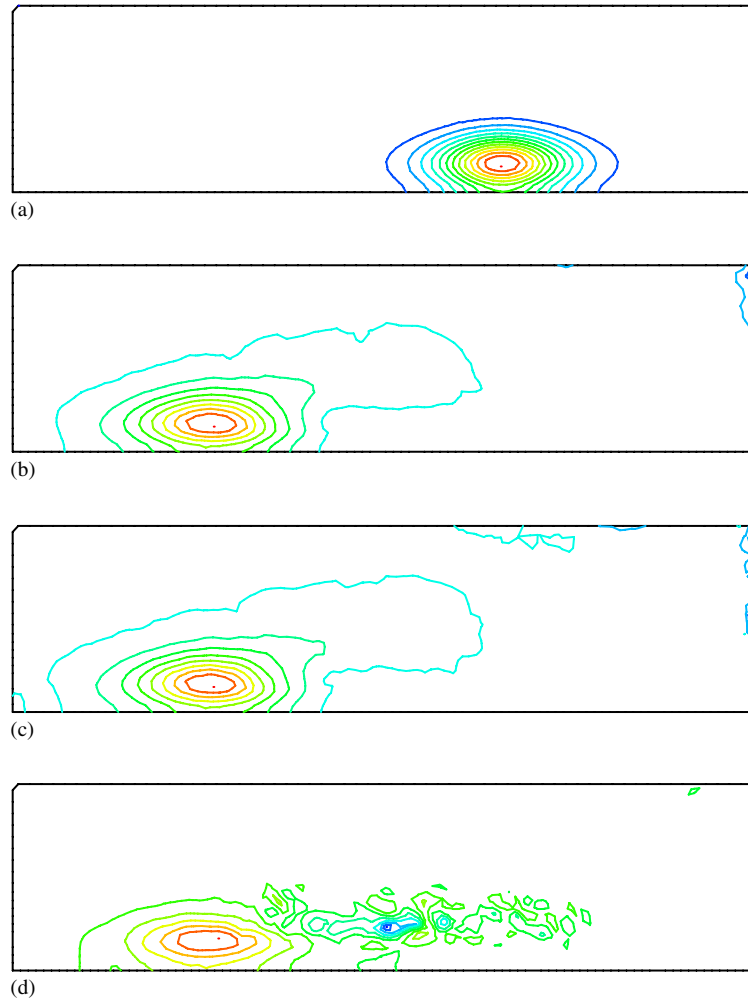


Figure 3. Isolines of the surface elevation for the ISLFEM after 55 days (32 adimensional time units) for the HCT-R, HCT-C, and Bell approximation schemes. The minimum (Min) and maximum (Max) values of the surface elevation are indicated: (a) initial solution, Min=0, Max=0.168; (b) HCT-R, Min=-0.038379, Max=0.11498; (c) HCT-C, Min=-0.03958, Max=0.11397; and (d) Bell, Min=-0.7824, Max=0.1784.

that certain observed features of the life cycle of anticyclonic eddies in the western Gulf should be simulated.

Equations (1) and (2) are solved with g replaced by g' subject to the no-normal-flow condition (4). A Gaussian distribution of η centered at the middle of the domain is prescribed at initial time

$$\eta(x, y, t=0) = C \exp(-D(x^2 + y^2)) \tag{30}$$

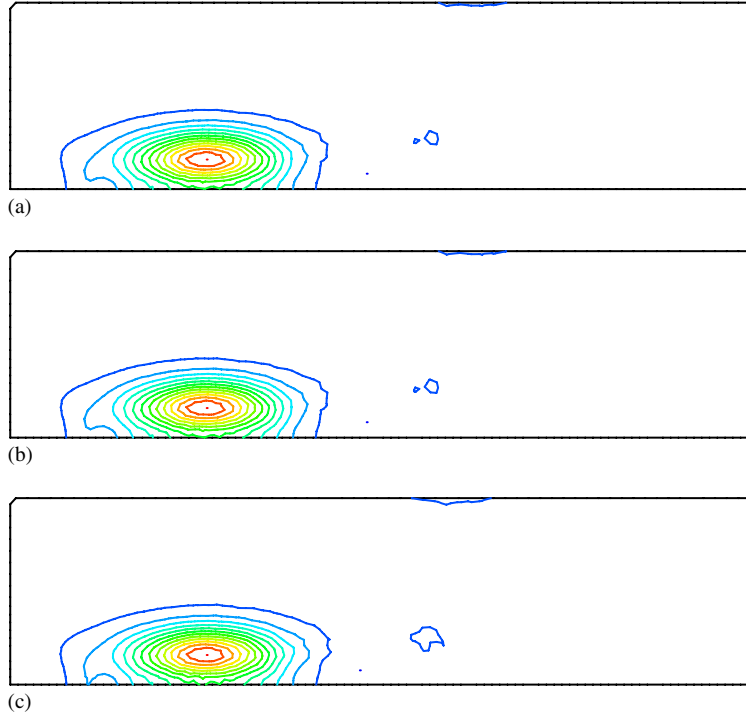


Figure 4. As for Figure 3 but for the QSLFEM: (a) HCT-R, Min = -0.00716, Max = 0.15912; (b) HCT-C, Min = -0.00714, Max = 0.15912; and (c) Bell, Min = -0.007359, Max = 0.15818.

Table I. The phase velocity for the ISLFEM and the QSLFEM using the HCT-R, HCT-C and Bell approximation schemes.

	ISLFEM	QSLFEM
HCT-R	0.6788	0.7977
HCT-C	0.6751	0.7977
Bell	0.8449	0.7954

and the initial anticyclonic velocity field is taken to be in the geostrophic equilibrium $\mathbf{k} \wedge \mathbf{u} = g' \nabla \eta$; hence,

$$\begin{aligned}
 u(x, y, t=0) &= \frac{2g'}{f} C D y \exp(-D(x^2 + y^2)) \\
 v(x, y, t=0) &= -\frac{2g'}{f} C D x \exp(-D(x^2 + y^2))
 \end{aligned}
 \tag{31}$$

where $C = 68.2 \text{ m}$ and $D = 5.92 \times 10^{-11} \text{ m}^{-2}$. The β -plane approximation is used where f_0 and β are evaluated at 25°N . We choose $g' = 1.37 \times 10^{-1} \text{ m s}^{-1}$ and $H = 100 \text{ m}$; hence, the mean gravity wave

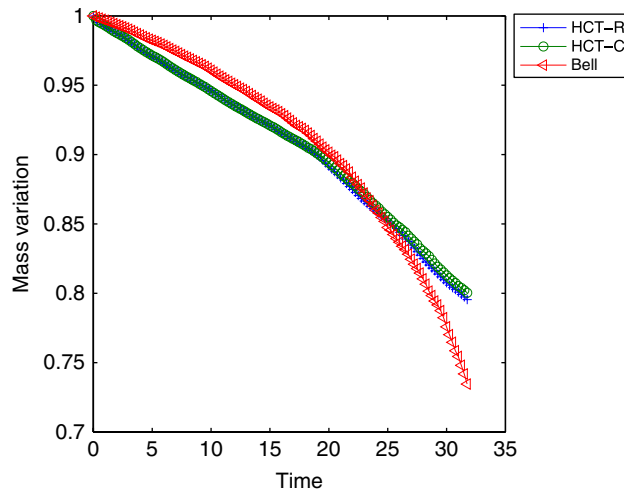


Figure 5. Mass variation as a function of time for the ISLFEM and the HCT-R, HCT-C and Bell schemes after 32 adimensional time units (55 days).

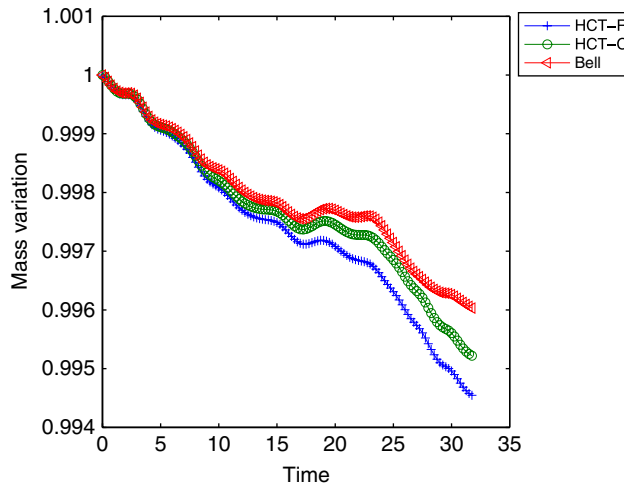


Figure 6. As for Figure 5 but for the QSLFEM.

speed is $\sqrt{g'H} \approx 3.7 \text{ ms}^{-1}$ and the radius of deformation at midbasin is $R_d = \sqrt{g'H}/f_0 \approx 60 \text{ km}$. The time step is 300 s and this choice yields the gravitational Courant number $\sqrt{g'H} \Delta t / h \approx 0.1$.

Simulation results are shown for the QSLFEM since for the ISLFEM after only one day of simulation, the eddy has lost more that 50% of its amplitude. The $P_1^{\text{NC}}-P_1$ and P_2-P_1 pairs are used, and the eddy is located at the center of the Gulf of Mexico at initial time. The geostrophic balance of the velocities imposed a readjustment of the flow toward a gradient wind balance on the β plane after flow's initialization. For this reason, η loses approximately 10% of its initial

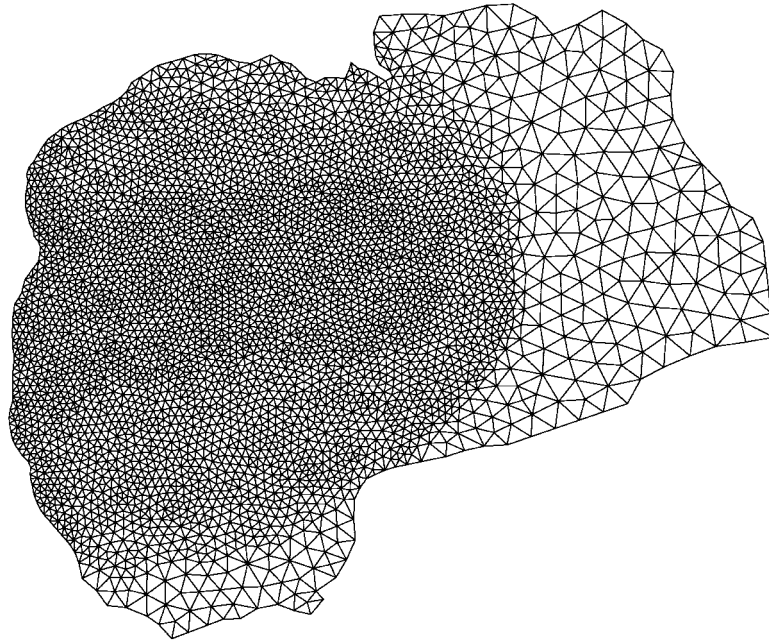


Figure 7. The unstructured mesh of the Gulf of Mexico: 8001 triangles, 4092 vertices, 12 092 edges. The mesh resolution is 20 km in the western part of the Gulf and 60 km in the eastern part.

amplitude for both pairs. However, this slight imbalance in the initial condition does not amplify during the simulation. The eddy migrate to the west and its westerly race exhibits a southwestern drift due to nonlinear effects. This is in agreement with the dynamic of Rossby waves.

5.2.1. The $P_1^{\text{NC}}-P_1$ approximation. Results for the $P_1^{\text{NC}}-P_1$ pair and the HCT-R, HCT-C and Bell \mathcal{C}^1 interpolating schemes are now discussed. The isolines of the surface elevation are shown in Figure 8 at different stages of the eddy propagation for the HCT-R approximation. Results for the HCT-C and Bell schemes are not shown since they are very similar to the HCT-R ones. However, the maximum and minimum values of the surface elevation are shown in Table II for the three schemes during the 11 weeks of simulation. The maximum values of the flow speed field are graphed in Figure 9.

After 11 weeks of simulation, the loss amplitude for η is 19.03, 18.9, and 14.07% for the HCT-R, HCT-C, and Bell approximations, respectively. The loss of amplitude for the flow speed field is 9.7 and 9.8% for the HCT-R and HCT-C schemes, respectively, and an increase of 2.5% for the Bell approximation. In [21], the use of the $P_1^{\text{NC}}-P_1$ pair and a kriging approach for the ISLFEM leads to a loss of amplitude of 22.31 and 14% for the surface elevation and flow speed field, respectively. However, the use of an Eulerian scheme in [21] (with the $P_1^{\text{NC}}-P_1$ pair) gives slightly better results since the loss of amplitude is only 15.26 and 6% for the elevation and flow speed field, respectively. Note that contrary to [21] there is no need to introduce an eddy-diffusion term in the present study for the semi-Lagrangian advection.

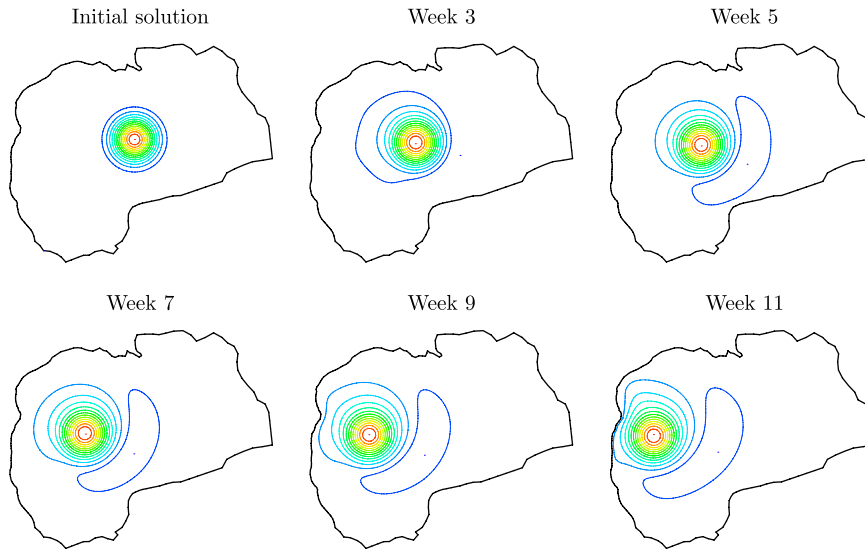


Figure 8. Isolines of the surface elevation at different times of the propagation for the $P_1^{NC}-P_1$ FE pair and the HCT-R approximation.

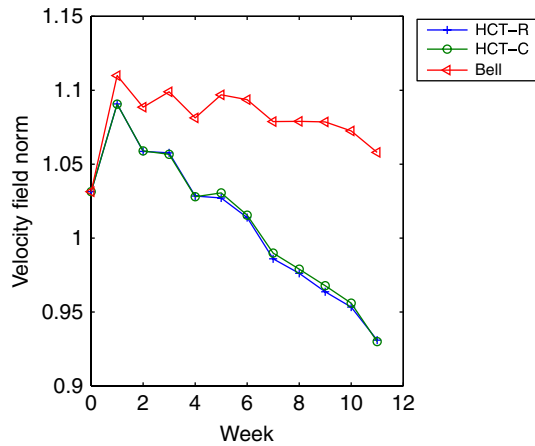


Figure 9. Maximum values of the flow speed field for the QSLFEM and the $P_1^{NC}-P_1$ FE pair during the propagation (11 weeks) for the HCT-R, HCT-C, and Bell approximation schemes.

As shown in Figure 10 the mass is well conserved after 11 weeks of simulation. We have $MV = 0.9917, 0.9924,$ and 0.9976 for the HCT-R, HCT-C, and Bell approximations, respectively. The loss of mass is thus less than 1% for the QSLFEM.

5.2.2. *The P_2-P_1 approximation.* Results for the P_2-P_1 pair and the HCT-R interpolating scheme are now analyzed. The results for the HCT-C are not presented since they are very similar to

Table II. Maximum and minimum values of the surface elevation and velocity fields for the QSLFEM and the $P_1^{\text{NC}}-P_1$ pairs using the HCT-R, HCT-C, and Bell approximation schemes and the P_2-P_1 pair using the HCT-R scheme.

Week	$P_1^{\text{NC}}-P_1$ (elevation)			P_2-P_1 (HCT-R)	
	HCT-R	HCT-C	Bell	Elevation	Velocity
1	60.925	60.952	61.296	60.688	1.083
	-1.355	-1.328	-1.460	-1.410	0
2	60.270	60.293	60.993	60.017	1.045
	-2.346	-2.343	-2.409	-2.374	0
3	59.301	59.297	60.204	58.387	1.040
	-3.532	-3.533	-3.627	-3.596	0
4	59.143	59.162	60.306	58.555	1.004
	-4.634	-4.651	-4.844	-4.661	0
5	58.185	58.185	59.772	57.468	0.995
	-5.392	-5.392	-5.518	-5.391	0
6	57.599	57.623	59.566	56.793	0.979
	-5.845	-5.870	-6.038	-5.893	0
7	57.042	57.077	59.197	56.169	0.948
	-6.176	-6.171	-6.230	-6.284	0
8	56.860	56.910	59.201	55.814	0.932
	-6.434	-6.432	-6.545	-6.563	0
9	56.860	56.338	59.061	55.044	0.922
	-6.444	-6.432	-6.453	-6.635	0
10	55.843	55.901	58.687	54.609	0.907
	-6.430	-6.401	-6.488	-6.643	0
11	55.216	55.301	58.600	53.885	0.885
	-6.405	-6.380	-6.488	-6.610	0

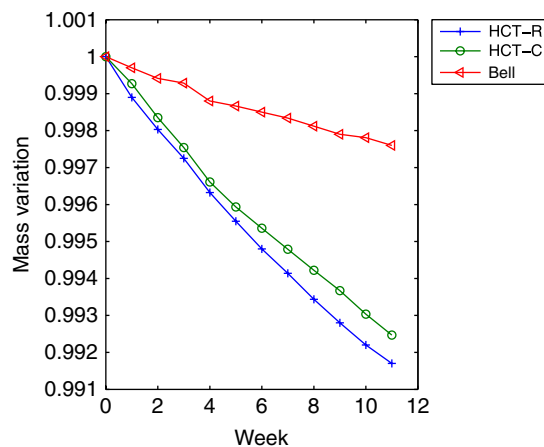


Figure 10. Mass variation for the QSLFEM and the $P_1^{\text{NC}}-P_1$ FE pair during the propagation (11 weeks) for the HCT-R, HCT-C, and Bell approximation schemes.

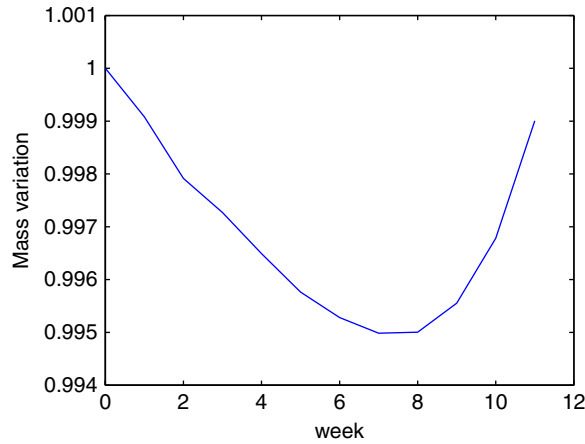


Figure 11. As for Figure 10 but for the P_2-P_1 FE pair and the HCT-R scheme.

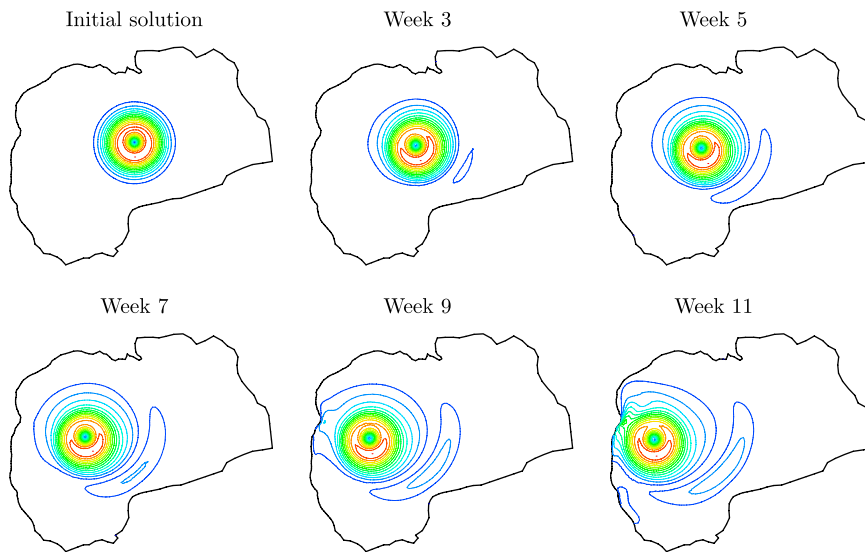


Figure 12. Isolines of the velocity field at different times of the propagation for the P_2-P_1 FE pair and the HCT-R approximation.

the HCT-R ones, as in the previous section. The isolines of the flow velocity field are shown in Figure 12 at different stages of the eddy propagation, and the Rossby wave dynamics is again well reproduced. The contour plots for the surface elevation are not shown since the results are very similar to those obtained in Figure 8 for the $P_1^{NC}-P_1$ pair. The maximum and minimum values of the elevation and flow speed field are presented in Table II during the simulation. The loss of amplitude is 20.98 and 14.19% for the elevation and flow speed field, respectively, after 11 weeks of propagation. Compared with the $P_1^{NC}-P_1$ results, the loss of amplitude for η is thus slightly

higher, but the damping is much severe for the flow speed field, although the approximation for velocity is quadratic for the P_2 – P_1 pair and linear for the P_1^{NC} – P_1 one. As shown in Figure 11, the mass is well conserved since we have $MV=0.999$ after 11 weeks of simulation.

6. CONCLUSION

The finite element, semi-implicit, and semi-Lagrangian advection methods have been successfully combined on unstructured meshes to solve the nonlinear shallow-water equations. Both continuous and discontinuous FE schemes are employed, namely the P_2 – P_1 and P_1^{NC} – P_1 pairs. In this paper, two semi-Lagrangian methods are considered by tracking the feet of the characteristic lines either from the interpolation (ISLFEM) or from the integration (QSLFEM) nodes. The \mathcal{C}^1 interpolating schemes for semi-Lagrangian advection include the Hsieh–Clough–Tocher FE reduced and complete and the Bell family.

Two test problems involve the propagation of an equatorial solitary Rossby wave and the evolution of an anticyclonic eddy at midlatitudes. The Rossby wave dynamics of the propagation is well simulated by the model for the QSLFEM, which provides an accurate computation of the Rossby modes. The Hsieh–Clough–Tocher interpolation schemes have been found more accurate than the Bell scheme. The mass is well conserved for both tests, since the loss of mass is less than 1% after few weeks of simulation. For the ISLFEM, the propagation is also well simulated but the method leads to overdamped results. Although the QSLFEM may lead to instabilities [25], such a difficulty has not been encountered in the present work. These encouraging results suggest undertaking further experiments with a realistic bathymetry and wind forcing.

ACKNOWLEDGEMENTS

This work was supported by grants from the Natural Sciences and Engineering Research Council (NSERC) and grants from the Fonds québécois de la recherche sur la nature et les technologies (FQRNT). The use of the computing facilities of the Groupe Interdisciplinaire de Recherche en Éléments Finis (GIREF) is also acknowledged.

REFERENCES

1. Bryan K. A numerical method for the study of the circulation of the world ocean. *Journal of Computational Physics* 1969; **4**:347–376.
2. Bryan K, Cox MD. A numerical investigation of the oceanic general circulation. *Tellus* 1967; **19**:54–80.
3. Le Provost C, Vincent P. Finite element for modeling ocean tides. In *Tidal Hydrodynamics*, Parker B (ed.). Wiley: New York, 1991; 41–60.
4. Westerink JJ, Gray WG. Progress in surface water modeling. *Reviews of Geophysics* 1991; **29**:210–217.
5. Lyard F, Lefevre F, Letellier T, Francis O. Modelling the global ocean tides: modern insights from FES2004. *Ocean Dynamics* 2006; **56**:394–415.
6. Iskandarani M, Haidvogel DB, Levin JC. A three dimensional spectral element method for the solution of the hydrostatic primitive equations. *Journal of Computational Physics* 2003; **186**:397–425.
7. Fringer OB, Gerritsen M, Street RL. An unstructured-grid, finite-volume, nonhydrostatic, parallel coastal ocean simulator. *Ocean Modelling* 2006; **14**:139–173.
8. Chen C, Liu H, Beardsley RC. An unstructured grid, finite volume, three dimensional, primitive equations ocean model: application to coastal ocean and estuaries. *Journal of Atmospheric and Oceanic Technology* 2003; **20**:159–186.

9. Lynch DR, Ip JTC, Naimie CE, Werner FE. Comprehensive coastal circulation model with application to the Gulf of Maine. *Continental Shelf Research* 1996; **16**:875–906.
10. Danilov S, Kivman G, Schröter J. A finite element ocean model: principles and evaluation. *Ocean Modelling* 2004; **6**:125–150.
11. White L, Deleersnijder E, Legat V. A three-dimensional unstructured mesh finite element marine model, with application to the flow around a shallow-water island. *Journal of Geophysical Research* 2006, submitted.
12. Piggott MD, Gorman GJ, Pain CC, Allison PA, Candy AS, Martin BT, Wells MR. A new computational framework for multi-scale ocean modelling based on adapting unstructured meshes. *International Journal for Numerical Methods in Fluids* 2007; DOI: 10.1002/fld.1663.
13. Cockburn B, Karniadakis GE, Shu CW. The development of discontinuous Galerkin methods. In *Discontinuous Galerkin Methods: Theory, Computation and Applications*, Cockburn B, Karniadakis G, Shu C-W (eds). Lecture Notes in Computer Science and Engineering, vol. 11. Springer: Berlin, 2000; 3–50.
14. Cockburn B, Shu CW. Runge–Kutta discontinuous Galerkin methods for convection-dominated problems. *Journal of Scientific Computing* 2001; **16**:173–261.
15. Blain CA, Massey TC. Application of a coupled discontinuous–continuous Galerkin finite element shallow water model to coastal ocean dynamics. *Ocean Modeling* 2005; **10**(3–4):283–315.
16. Dawson C, Westerink JJ, Pothina D, Feyen J. Continuous, discontinuous, and coupled discontinuous–continuous Galerkin finite element methods for the shallow water equations. *International Journal for Numerical Methods in Fluids* 2006; **52**(1):63–88.
17. Dawson C, Proft J. Coupled discontinuous and continuous Galerkin finite element methods for the depth-integrated shallow-water equations. *Computer Methods in Applied Mechanics and Engineering* 2004; **193**:289–318.
18. Khanta LH, Clayson CA. Numerical models of ocean and oceanic processes. *International Geophysics Series*. Academic Press: New York, 2000.
19. Hanert E, Le Roux DY, Legat V, Deleersnijder E. Advection schemes for unstructured grid ocean modelling. *Ocean Modelling* 2004; **7**:39–58.
20. Walters RA, Casulli V. A robust finite element model for hydrostatic surface water flows. *Communications in Numerical Methods in Engineering* 1998; **14**:931–940.
21. Hanert E, Le Roux DY, Legat V, Deleersnijder E. An efficient Eulerian finite-element method for the shallow-water equations. *Ocean Modelling* 2005; **10**:115–136.
22. Le Roux DY. Dispersion relation analysis of the $P_1^{\text{NC}}-P_1$ finite-element pair in shallow water models. *SIAM Journal on Computing* 2005; **27**:394–414.
23. Le Roux DY, Rostand V, Pouliot B. Analysis of numerically-induced oscillations in 2D finite-element shallow-water models. Part I: inertia-gravity waves. *SIAM Journal on Scientific Computing* 2007; **29**:331–360.
24. Le Roux DY, Pouliot B. Analysis of numerically-induced oscillations in 2D finite-element shallow-water models. Part II: free planetary waves. *SIAM Journal on Scientific Computing* 2007; submitted.
25. Djoumna G, Pierre R, Le Roux DY. High order \mathcal{C}^1 finite-element interpolating schemes. Part I: semi-Lagrangian linear advection. *International Journal for Numerical Methods in Engineering* 2007; DOI: 10.1002/fld.1688.
26. Le Roux DY, Lin AC, Staniforth A. A semi-implicit semi-Lagrangian finite-element shallow-water ocean-model. *Monthly Weather Review* 2000; **128**:1384–1401.
27. Pedlosky J. *Geophysical Fluid Dynamics*. Springer: Berlin, 1998.
28. Robert A. A stable numerical integration scheme for the primitive meteorological equations. *Atmosphere-Ocean* 1981; **19**:35–46.
29. Robert A. A semi-Lagrangian and semi-implicit numerical integration scheme for the primitive meteorological equations. *Japan Meteorological Society* 1982; **60**:319–325.
30. Le Roux DY, Staniforth A, Lin AC. Finite element for shallow-water equation ocean models. *Monthly Weather Review* 1998; **126**:1931–1951.
31. Bates JR, McDonald A. Multiply-upstream, semi-Lagrangian advective schemes: analysis and application to a multilevel primitive equation. *Monthly Weather Review* 1982; **11**:1831–1842.
32. Temperton C, Staniforth A. An efficient two-time level semi-Lagrangian semi-implicit integration scheme. *Quarterly Journal of the Royal Meteorological Society* 1987; **113**:1025–1039.
33. Hood P, Taylor C. Navier–Stokes equations using mixed interpolation. In *Finite Elements in Flow Problems*, Oden JT *et al.* (eds). The University of Alabama in Huntsville (UAH) Press: Huntsville, AL 35899, U.S.A., 1974; 121–132.
34. Hua BL, Thomasset F. A noise-free finite-element scheme for the two-layer shallow-water equations. *Tellus* 1984; **36A**:157–165.

35. Pudykiewicz J, Staniforth A. Some properties and comparative performances of the semi-Lagrangian method in the solution of the advection–diffusion equation. *Atmosphere-Ocean* 1984; 283–308.
36. Purser RJ, Leslie LM. A semi-implicit semi-Lagrangian finite difference scheme using high order spatial differencing on a nonstaggered grid. *Monthly Weather Review* 1988; **116**:2069–2080.
37. Le Roux DY, Lin AC, Staniforth A. An accurate interpolating scheme for semi-Lagrangian advection on an unstructured mesh for ocean modelling. *Tellus* 1997; **49**:119–138.
38. Gray WG. On the normal boundary conditions in finite element codes for two-dimensional shallow water flow. *International Journal for Numerical Methods in Fluids* 1984; **4**:99–104.
39. Engelman MS, Sani RL, Gresho PM. The implementation of normal/or tangential boundary conditions in finite-element codes for incompressible fluid flow. *International Journal for Numerical Methods in Fluids* 1982; **2**:225–238.
40. Boyd JP. Equatorial solitary waves. Part I: Rossby solitons. *Journal of Physical Oceanography* 1980; **10**:1699–1717.